Engineering xxx (xxxx) xxx

Contents lists available at ScienceDirect

Engineering

journal homepage: www.elsevier.com/locate/eng

Research
Mechanical Engineering—Article

Microfabricated Atomic Vapor Cells with Multi-Optical Channels Based on an Innovative Inner-Sidewall Molding Process

Mingzhi Yu [a,b], Yao Chen [a,b,c,*], Yongliang Wang [d], Xiangguang Han [a,b,c], Guoxi Luo [a,b,c], Libo Zhao [a,b,c,*], Yanbin Wang [a,b], Yintao Ma [a,b], Shun Lu [a,b], Ping Yang [a,b,c], Qijing Lin [a,b,c], Kaifei Wang [e,*], Zhuangde Jiang [a,b,c]

[a] International Joint Laboratory for Micro/Nano Manufacturing and Measurement Technologies, Xi'an Jiaotong University, Xi'an 710049, China
[b] School of Mechanical Engineering, Xi'an Jiaotong University, Xi'an 710049, China
[c] Shandong Laboratory of Yantai Advanced Materials and Green Manufacturing, Yantai 265503, China
[d] Moon Environment Technology Co., Ltd., Yantai 264000, China
[e] Emergency Department, The First Affiliated Hospital of Xi'an Jiaotong University, Xi'an 710061, China

ARTICLE INFO

Article history:
Available online xxxx

Keywords:
Microfabricated atomic vapor cells
Inner-sidewall molding
Multiple optical channels
Quantum sensing

ABSTRACT

Existing microfabricated atomic vapor cells have only one optical channel, which is insufficient for supporting the multiple orthogonal beams required by atomic devices. In this study, we present a novel wafer-level manufacturing process for fabricating multi-optical-channel atomic vapor cells and an innovative method for batch processing the inner sidewalls of millimeter glass holes to meet optical channel requirements. Surface characterization and transmittance tests demonstrate that the processed inner sidewalls satisfy the criteria for an optical channel. In addition, the construction of an integrated processing platform enables multilayer non-isothermal anode bonding, the filling of inert gases, and the recovery and recycling of noble gases. Measurements of the absorption spectra and free-induction decay signals of xenon-129 (^{129}Xe) and xenon-131 (^{131}Xe) under different pump-probe schemes demonstrate the suitability of our vapor cell for use in atomic devices including atomic gyroscopes, dual-beam atomic magnetometers, and other optical/atomic devices. The proposed micromolding technology has broad application prospects in the field of optical-device processing.

1. Introduction

With the advent of quantum technology, precision measurement devices based on quantum phenomena have been extensively studied [1–3]. Examples of such instruments include superconducting quantum interference devices (SQUIDs) [4,5] and optically pumped magnetometers (OPMs) [6,7]. Alkali metal atomic vapor cells, which are sealed with alkali metals and a specific volume of noble gas, are the core components of quantum devices such as atomic clocks [8–10], atomic magnetometers [11–13], and atomic gyroscopes [14,15].

Traditional alkali metal atomic vapor cells are manufactured using the glass-blowing method [16–18], which is expensive, poses difficulties in batch production, and does not guarantee consistency. In the glass-blowing method, a stem of a few millimeters is attached to the vapor cell, increasing the quadrupole frequency shift when the atomic nuclear spin $I \geq 1$ [19,20]. This occurs with xenon-131 (^{131}Xe), hydrargyrum-201 (^{201}Hg), krypton-83 (^{83}Kr), and neon-21 (^{21}Ne), causing the primary systematic errors that limit the bias stability in nuclear magnetic resonance (NMR) gyroscopes [21]. Moreover, traditionally fabricated alkali metal atomic vapor cells are incompatible with microelectromechanical systems (MEMSs) and cannot be applied to chip-scale atomic devices. Wafer-level fabrication makes it possible to achieve MEMS alkali metal vapor cells with sufficient miniaturization, low power consumption, and low manufacturing costs [22]. In addition, in microfabricated MEMS vapor cells, having no stem can reduce the quadrupole frequency shift [20,23,24].

The MEMS alkali metal vapor cell was first proposed by Kitching et al. [25]. During the early development of the MEMS vapor cell [26–31], it had only two transparency windows. In spin-exchange relaxation-free atomic magnetometers or atomic spin

* Corresponding authors.
E-mail addresses: yaochen@xjtu.edu.cn (Y. Chen), libozhao@xjtu.edu.cn (L. Zhao), kaifeiw@xjtufh.edu.cn (K. Wang).

https://doi.org/10.1016/j.eng.2023.08.016

Please cite this article as: M. Yu, Y. Chen, Y. Wang et al., Microfabricated Atomic Vapor Cells with Multi-Optical Channels Based on an Innovative Inner-Sidewall Molding Process, Engineering, https://doi.org/10.1016/j.eng.2023.08.016

gyroscopes, multi-beam configurations are required to achieve better performance [11,32,33]. Therefore, developing multi-beam MEMS vapor cells for chip-scale atomic devices is necessary.

Based on a wafer-level glass-blowing procedure, Eklund et al. [34,35] developed a MEMS spherical alkali metal atomic vapor cell. Although a multi-beam optical channel was enabled, the laser beam diverged because of the nonuniform wall thickness of the spherical vapor cell. Divergence of the laser beam may reduce spin polarization. Mirrors built into the cavities offer an alternative solution. Perez et al. [36,37] fabricated a Bragg reflector on the inclined sidewall of a cavity using bulk silicon (Si) micromachining and multilayer plasma-enhanced chemical vapor deposition. The laser beam flowing through the cavity was redirected to the light source plane. However, the uneven thickness of the deposited Bragg reflector resulted in inconsistent reflectivity and higher angle accuracy requirements for laser incidence. Han et al. [38] built a vapor cell with an aluminum reflection sidewall; however, the aforementioned issues persisted, despite the relative simplicity of the production process. Moreover, in an NMR gyroscope, a vapor cell with reflective sidewalls disrupts the symmetry of the vapor cell, resulting in a frequency shift of ^{131}Xe caused by nuclear quadrupole interaction. In summary, although researchers have investigated a number of solutions, the batch fabrication of atomic vapor cells with multiple optical channels based on the MEMS process still has the drawbacks of complex fabrication, irregular chamber shapes, the introduction of metal impurities, and high requirements for external laser incidence accuracy.

In this study, we develop a side-molding process to fabricate glass cavities with high-quality inner sidewalls in order to facilitate the mass production of MEMS multi-optical-channel alkali metal atomic vapor cells. In this process, a mold with a smooth surface is plugged into the glass cavity, and the mold and inner sidewalls squeeze each other at a specific viscoelastic temperature, such that the rough sidewalls of the glass cavity are deformed into an optical plane. Using this technique, an atomic vapor cell with multiple optical channels is fabricated, and its effectiveness is demonstrated through a series of optical tests. Platforms for testing the vapor cell are also developed to acquire the free-induction decay (FID) signal and the relaxation times of xenon-129 (^{129}Xe) and ^{131}Xe.

2. Methods

2.1. Structure design

The structure of the MEMS vapor cell is shown in Fig. 1. It is composed of top glass, Si, middle glass, Si, and bottom glass, which are connected using anodic bonding technology. The thicknesses of the top and bottom glasses are 500 μm, the thickness of the middle glass is 2 mm, and the Si is p-type (100)-oriented high-resistance monocrystalline Si with a thickness of 500 μm. SCHOTT BOROFLOAT®33 (BF33) glass is used.

The total size of the vapor cell is 5 mm × 5 mm × 4 mm, and the internal cavity size is 3 mm × 3 mm × 3 mm. The cavities contain rubidium (Rb), nitrogen gas (N_2), ^{129}Xe, and ^{131}Xe. After precision-side molding, the vapor cell has three optical channels through which three orthogonal laser beams pass.

2.2. Inner sidewall molding

Optical glass molding technology is based on continuous and reversible thermal processes, with glass properties varying from the molten to the solid state [39]. Near the glass transition temperature, the glass and aluminum oxide (Al_2O_3) molds were heated and pressurized under oxygen-free conditions, and the glass was molded into optical components. Compared with the traditional molding process, which requires pressure to deform the glass, we used the thermal expansion of the mold and glass to cause them to squeeze each other. Subsequently, the high-precision surface of the Al_2O_3 mold was copied onto a glass surface. Thus, the glass surface satisfies the optical interface requirements.

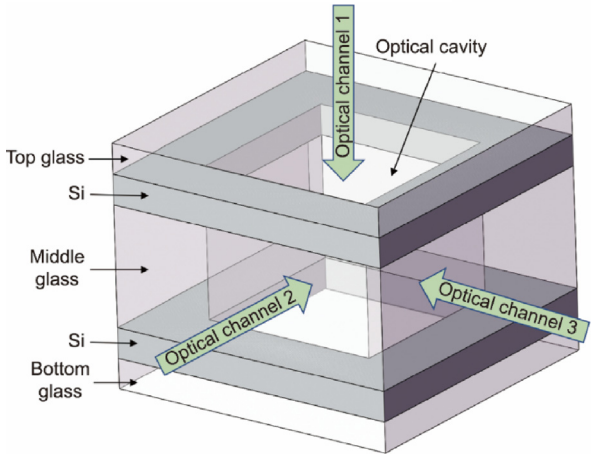

Fig. 1. An alkali metal vapor cell structure with multiple optical channels.

Compared with the traditional molding process, this process has several advantages: First, it can remove the inner surface morphology, whereas traditional molding processes cannot. Second, the glass deformation is minimal (only a few tens of microns) when the thermal expansion of the material is used during extrusion molding; thus, the internal stresses generated in the glass are miniscule, and the optical properties of the glass, such as the refractive index, are maintained. Third, no molding pressure is applied, indicating that mold damage is minor, which is conducive to mold recycling and results in reduced cost.

Fig. 2 shows the fabrication process of the MEMS multi-optical-channel alkali metal atomic vapor cells. The treatment steps for the inner sidewall are shown in Fig. 2(a)–(f). Fig. 2(a) depicts the laser drilling of a glass wafer with a drilling size of 3 mm × 3 mm and a depth of 2 mm. Because the efficiency of the laser process for fabricating deep holes is much greater than that of wet or dry etching using MEMS technology, the laser process was used to fabricate deeper cavities. The parameters used for the laser drilling are listed in Table 1.

Fig. 3 shows the pictures of MEMS atomic vapor cell wafers after different process treatments. A glass wafer fabricated by means of laser drilling is shown in Fig. 3(a). After testing, the precision of the drilling size was greater than 5 μm, the surface roughness of the inner sidewall was less than 5 μm, and the inner sidewall steepness was 90° ± 0.2°. Thus, this treatment method has high processing efficiency, high dimensional accuracy, and high angular accuracy. Even though the edges of the holes have defects that are several tens of microns wide, they do not have any bumps; therefore, anodic bonding is unaffected.

Fig. 2(b) shows the etching of Si holes using inductively coupled plasma (ICP) etching. The size of the Si hole is slightly larger (by several microns) than that of the glass hole to prevent extrusion of the Si and α-Al_2O_3 molds during molding. Fig. 2(c) depicts the first anodic bonding of the etched Si wafers and the laser-drilled glass wafer. The bonding voltage was 800 V, and the temperature was 400 °C.

Fig. 2(d) shows that a layer of metal was sputtered on the peripheral side of the previously bonded wafer as a side lead to ensure proper voltage during anode bonding between the middle glass layer and the lower Si layer. A Si wafer was bonded to the other glass side, with the same bonding parameters as those

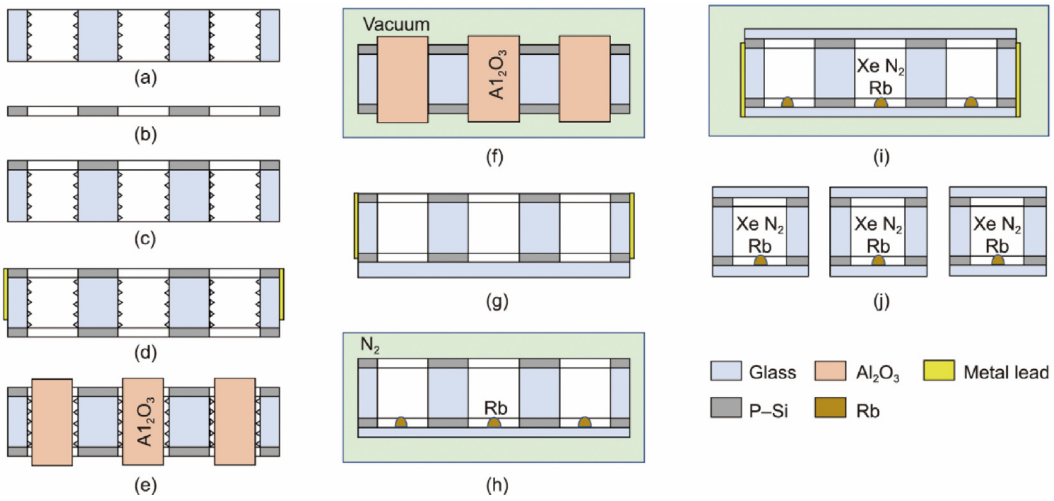

Fig. 2. Fabrication process of MEMS multi-optical-channel alkali metal atomic vapor cells. (a) Laser drilling the glass wafers. (b) Inductively coupled plasma (ICP) etching of a Si wafer. (c) First anodic bonding of Si to the middle glass. (d) Second anodic bonding of Si to the middle glass. (e) Placing the Al_2O_3 molds into the previously bonded wafer holes. (f) Heating the wafer and mold under vacuum for side molding. (g) Anodic bonding of the molded wafer to the bottom glass. (h) Alkali metal injection. (i) Filling the buffer gas and bonding the wafer to the top glass. (j) Splitting the alkali metal vapor cell wafer.

Table 1
Parameters used for laser drilling.

Items	Value
Power	3.5 W
Frequency	40.0 kHz
Pulse width	9.8 ns
Wavelength	532.0 nm
Single pulse energy	87.0 μJ

previously described. The bonded Si–glass–Si wafer is shown in Fig. 3(b), and its cross-sectional view is shown in Fig. 3(c).

Fig. 2(e) shows the mold preparation process. First, the bonded Si–glass–Si wafer was etched in an aqueous solution of 5% HCl, 30% HF, and 10% 3-indolepropionic acid for 15 min to remove the burrs and smooth the inner surfaces of the laser-drilled holes. The bonded wafer was cleaned with deionized water and dried with N_2. The α-Al_2O_3 molds were placed in the holes, as shown in Fig. 3(d). Wet etching improved the consistency of the sidewall roughness such that the mold would not be scratched by the glass sidewall when it was positioned, ensuring the reuse of the mold.

The dimensional accuracy of the α-Al_2O_3 molds was ± 1 μm, the surface shape accuracy PV was greater than $\lambda/4$ (λ = 632.8 nm, the surface shape accuracy PV was measured using a laser interferometer whose light source was a He–Ne laser with a wavelength of 632.8 nm), and the surface roughness was less than 10 nm. The reasons for choosing α-Al_2O_3 as the mold are as follows: This material has good high-temperature resistance, wear resistance, and chemical stability; high hardness and elastic modulus; and very low glass reactivity and glass bonding propensity [40]. Compared with the tungsten carbide mold used in traditional molding, Al_2O_3 has a large thermal expansion coefficient, which is beneficial for molding during thermal expansion.

The viscosity–temperature curve of BF33 glass can be obtained from Schott's official website [41], and the main viscosity points are listed in Table 2.

The distance between the mold and the inner sidewalls of the glass holes should be appropriate. A mold that is too large is not conducive to demolding, whereas a mold that is too small will lack sufficient mold pressure. During heating, the distance between the mold and the inner sidewalls of the glass holes (D_1) changes due to thermal expansion, as given by the following equation:

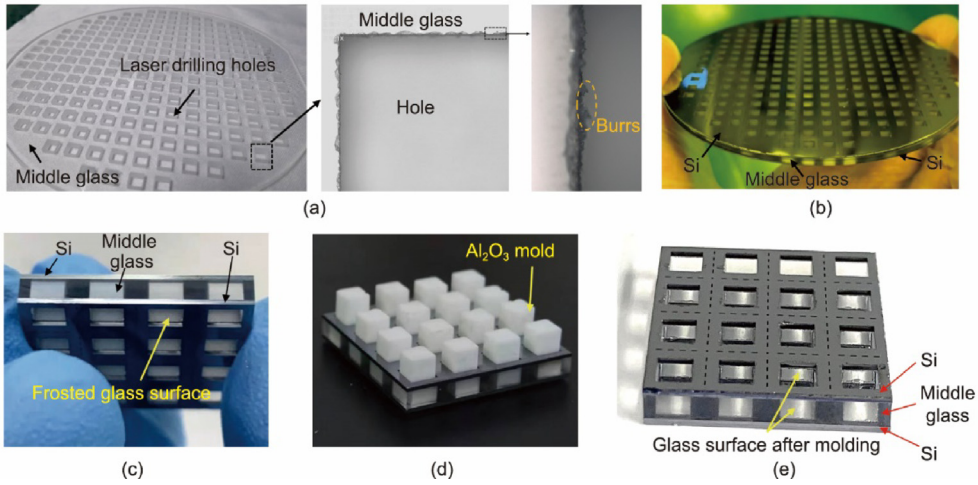

Fig. 3. Wafer pictures during processing. (a) Glass wafer after laser drilling. (b) Si–glass–Si wafer after second anodic bonding. (c) Si–glass–Si wafer cross-section. (d) Placing alumina molds into Si–glass–Si wafers. (e) Si–glass–Si wafer after inner sidewall molding.

Table 2
Relevant viscosity points of BF33 glass.

Viscosity point	Viscosity (dPa·s)	Temperature (K)
Strain point T_{st}	$10^{14.5}$	791
Transition point T_g	10^{14}	798
Annealing point T_a	10^{13}	833
Softening point T_s	$10^{7.6}$	1093
Working point T_w	10^{4}	1543

$$D_1 = \alpha_1 L_1 T_m + \alpha_2 L_2 T_m \quad (1)$$

where T_m is the molding temperature, which is generally between transition point T_g and softening point T_s. From Table 2, the range of T_m is 873–1123 K, while $\alpha_1 = (7.85 \pm 0.02) \times 10^{-6}$ K^{-1} is the average linear expansion coefficient of α-Al_2O_3. $L_1 = (3000 \pm 1)$ μm is the size of the α-Al_2O_3 molds, and α_2 is the thermal expansion coefficient of BF33 glass. The specific value of α_2 can be obtained from the official Schott website [41], where $L_2 = 2$ mm is the total thickness of the middle glass, due to the nonlinear deformation of the glass above $T_g = 798$ K. In this configuration, $D_1 = 29.0$–37.4 μm. Therefore, the mold size L_1 is several microns smaller than the cavity size of the vapor cell, so molding can still be achieved. After the measurement, the actual size of the hole was (3000 ± 5) μm. Therefore, we fabricated five types of molds with side lengths of 2990, 2985, 2980, 2975, and 2970 μm to determine the appropriate mold size.

Fig. 2(f) shows the molding steps. The wafer bonded to the molds was placed in a furnace and molded under vacuum. As shown in Fig. 2(c) and (d), Si wafers were bonded in advance on both sides of the middle glass, effectively preventing nonlinear deformation of the middle glass at high temperatures, to ensure the flatness of the upper and lower sides of the bonded wafer. Thus, the mold pressure did not affect the subsequent anodic bonding.

The molding experiment was performed using the temperature curve shown in Fig. 4. First, the temperature was raised to the molding temperature of T_m at a rate of 20 °C·min^{-1}. Then, the inner sidewalls of the middle glass holes were fully molded by remaining at T_m for 15 min. Afterward, the sample was cooled to the annealing temperature T_a at 5 °C·min^{-1} and held at that temperature for 30 min to eliminate the internal stresses of the glass. Finally, the sample was cooled to room temperature at 10 °C·min^{-1}. Two temperature cycles were performed in each molding experiment. The mold and glass naturally separated, making demolding easy, due to the shrinkage of the mold and the glass after cooling. Fig. 3(e) shows the cross section of a Si–glass–Si wafer after the inner sidewall molding.

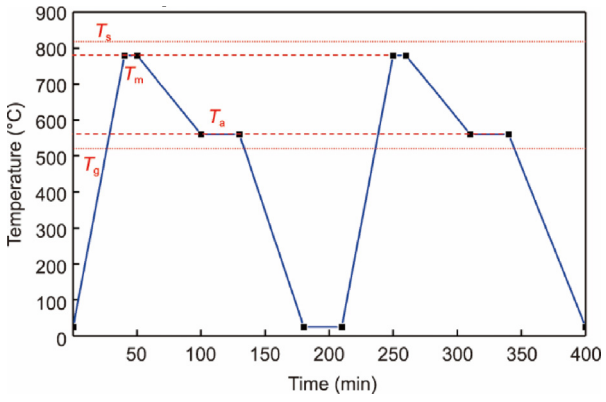

Fig. 4. Molding temperature as a function of time.

3. Results

3.1. Optimization of the Al_2O_3 mold size and molding temperature

As shown in Fig. 5, we studied the average surface roughness Sa of the inner sidewall of the middle glass hole at various mold sizes and temperatures to determine the appropriate optimal mold size and temperature T_m. Because the longitudinal coordinates were large, it was not possible to mark the roughness error for multiple samples with the same mold size and temperature. The average roughness values are shown in Fig. 5. The roughness of the inner sidewalls of the molded glass holes gradually decreased as the mold size and temperature increased. However, a mold that is excessively large can easily cause adhesion between the mold and the glass, resulting in molding failure. The 2985 μm mold adhered to the glass at temperatures greater than 775 °C, resulting in the inability to obtain roughness data. The 2990 μm mold could not be used, because it could not be smoothly placed in the glass holes.

In addition, adhesion was inevitable when the molding temperature exceeded the softening point temperature T_s. When the mold size was too small, the molding process was insufficient, indicating that Sa did not meet the application requirements. In summary, we chose a 2980 μm mold for molding at 790 °C; this achieved the best roughness, because it eliminated adhesion between the mold and the glass hole, which will be discussed in detail in the next section.

3.2. Surface characterization of the molded inner sidewalls of the middle glass holes

Fig. 6 shows the inner sidewall surface morphologies of the glass holes before and after molding using laser scanning confocal microscopy. The size of the sampling area is 640 μm × 640 μm. The inner sidewall was ground glass before molding, as shown in Figs. 6 (a) and (b). As shown in Table 3, the average surface roughness Sa of the sidewall surface was 5.653 μm, the average surface shape accuracy PV was approximately 67.304 μm, and the average kurtosis Sku was 6.236. The parameter Sku was used to determine the sharpness of the rough shape [42], as shown in Fig. 7. Many sharp peaks (i.e., burrs) were observed on the surface, as shown in Fig. 6 (b).

As shown in Table 3, after wet etching, Sa was 3.630 μm, the PV was 38.379 μm, and Sku was 3.154. The sharp part of the surface

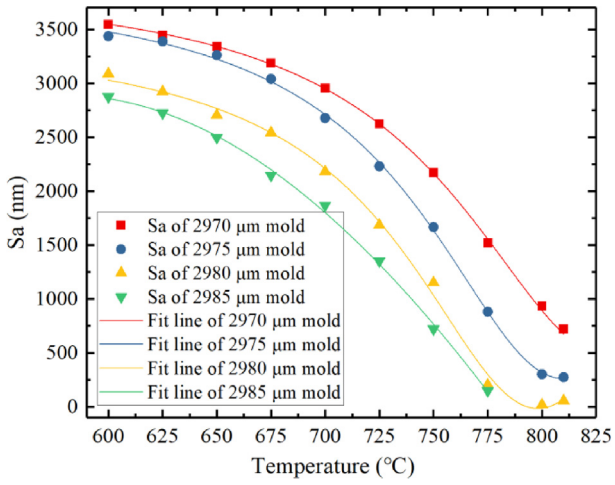

Fig. 5. Influence of mold size and molding temperature on the average surface roughness of the inner sidewalls of the middle glass holes.

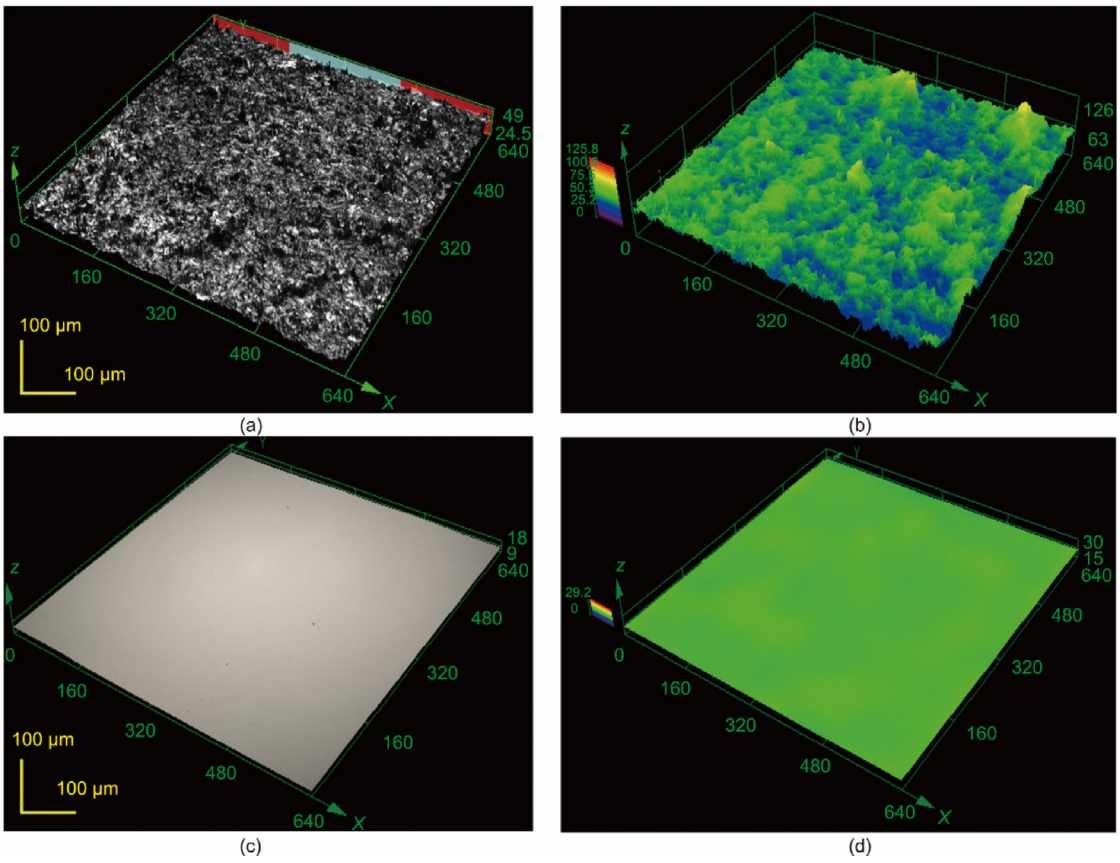

Fig. 6. Morphologies of the inner sidewalls of the middle glass holes using a laser scanning confocal microscope. (a) Morphology before molding. (b) Three-dimensional topography before molding. (c) Morphology after molding. (d) Three-dimensional topography after molding.

Table 3
Average surface parameters of different processes.

Procedure	Sa (μm)	PV (μm)	Sku
Laser drilling	5.653	67.304	6.236
Wet etching	3.630	38.379	3.154
After molding	0.022	0.283	2.506

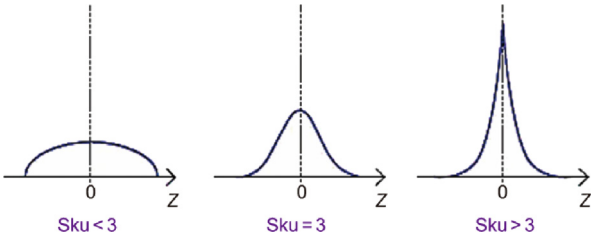

Fig. 7. Schematic diagram of the sharpness of the surface roughness is represented by Sku [42].

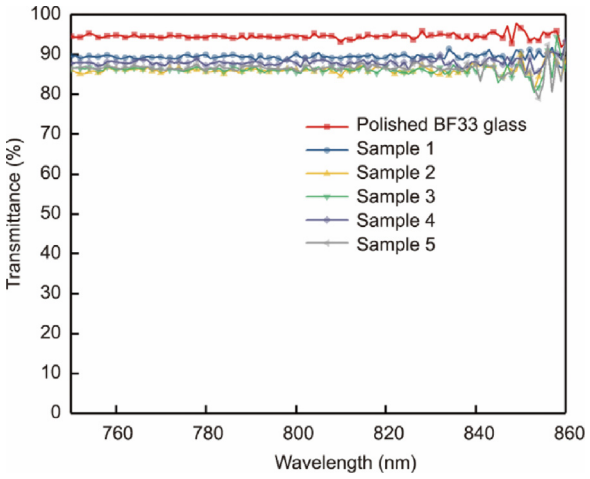

Fig. 8. Transmittances of the inner sidewalls of the glass holes after molding, as measured by a spectrophotometer.

burr was removed, and the surface roughness was relatively mild. Thus, wet etching can help improve the quality of molding and prevent burr scratching.

Figs. 6(c) and (d) show the surface morphology and three-dimensional (3D) topography after final molding. As shown in Table 3, Sa was 22 nm, the PV was 283 nm (less than $\lambda/2$), and Sku was 2.506.

An infrared–visible–ultraviolet spectrophotometer was used to measure the transmittance of the molded inner sidewalls of the glass holes in the near-infrared band, as shown in Fig. 8. The red curve at the top represents the transmittance of the polished glass, which has an average transmittance of approximately 94%. The five samples shown in Fig. 8 were collected from various parts of the wafer, ranging from the edge to the center. Their transmittance was not significantly correlated with the distribution location and fluctuated between 87% and 91% after measuring different batches of wafers, indicating that the molded inner sidewalls satisfied the requirements of the optical channel of the vapor cell.

3.3. Multilayer anodic bonding

As shown in Fig. 2(g), the peripheral edges of the two Si layers of the molded wafer were connected via magnetron sputtering with a metal. Then, the bottom glass was connected to the molded wafer via anodic bonding. Fig. 2(h) shows how the molten alkali metal was injected into the vapor cell using a micropipette in a N_2 environment.

As shown in Fig. 2(i), the top glass and the molded wafer with the alkali metal were placed in the bonding cavity. The bonding cavity was vacuumed to 1×10^{-5} mbar (1 mbar = 100 Pa), and 5 Torr (1 Torr = 133.3224 Pa) ^{129}Xe, 15 Torr ^{131}Xe, and 600 Torr N_2 were added to the bonding cavity. Subsequently, the upper plate of the anodic bonding equipment was pressed down to enable non-isothermal bonding. The temperatures of the upper and lower plates were 280 and 200 °C, respectively. The bonding voltage was 1200 V, and the duration was 120 min. The purpose of this step was to maintain the alkali metal at the bottom glass based on the temperature gradient to prevent it from affecting the bonding surfaces, thereby achieving a preliminary sealing of the vapor cell. Isothermal anodic bonding was also conducted. The temperatures of the upper and lower plates were both 280 °C, the bonding voltage was 1200 V, and the duration was 60 min to improve bonding strength and hermeticity.

A manufacturing platform with vapor cell bonding, gas filling, and noble gas recovery capabilities is shown in Fig. 9. The bonding cavity was placed on a platform in an inert gas glovebox. During the fabrication of the vapor cell, ^{129}Xe and ^{131}Xe, which are expensive, were selected as noble gases, and the volume of the bonding cavity was relatively large. We calculated that only about one thousandth of the Xe gas that filled the bonding chamber was sealed in the vapor cell each time. If noble gases are used only once, the processing costs will be high; therefore, it was necessary to design a gas-recovery system to reduce the manufacturing cost. In the recovery system, liquid nitrogen was used to cool the recovered gas mixture, the cheap nitrogen in the gas was liquefied, and the valuable Xe gas was stored in a cylinder for subsequent use.

A resin-bonded blade (i.e., a soft blade) with a 2000 mesh diamond surface was used for the wafer dicing. A high rotational speed and a low feed rate were used to cut the wafers with a good polishing effect on the cut surface. The surface roughness (R_a = (28 ± 5) nm) and face shape accuracy (PV = (180 ± 60) nm) were measured on the side of the cut wafer using a laser confocal microscope. The sample satisfied optical port quality requirements without additional polishing. Therefore, high efficiency of batch processing was ensured in this study.

The finished wafer containing Rb, ^{129}Xe, ^{131}Xe, and N_2 is shown in Fig. 10(a). There were 236 vapor cells in the 4 in (1 in = 2.54 cm) wafer. A local magnification of the wafer is shown in Fig. 10(b), with the Rb clearly visible. As shown in Fig. 10(c), the segmented alkali metal atomic vapor cell has three optical channels, numbered 1, 2, and 3. The chip size is 5 mm × 5 mm × 4 mm, and the internal cavity size is 3 mm × 3 mm × 3 mm, meeting the requirements for the miniaturization and batch manufacturing of quantum devices such as atomic magnetometers and atomic gyroscopes with multiple laser channels.

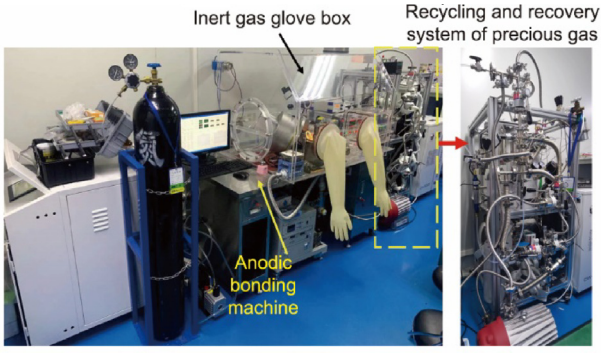

Fig. 9. The manufacturing platform.

3.4. Leakage rate

First, the hermeticity of the vapor cell was evaluated based on the leakage rate. The following method based on the MILSTD-883E standard method 1014.10 was used to measure the leakage rate: the vapor cell was placed in a sealed chamber, which was pressurized with helium (He) to pressure of exposure (P_E) = 5.17 × 10^5 Pa and maintained at this pressure for T_1 = 7200 s while keeping the temperature constant at 25 °C. Subsequently, the vapor cell was removed from the chamber and purged with N_2 to remove the surface He. Next, the vapor cell was quickly placed in a helium mass spectrometer (ASM310; PFEIFFER VACUUM, Germany) to measure the amount of diffused He. The volume of the vapor cell was approximately V = 27 mm^3, and the leakage rate of the vapor cell was calculated. The measured leak rate detected by the helium mass spectrometer leak detector was R_1 = 4.4 × 10^{-10} Pa·m^3·s^{-1}, and the equivalent standard leak rate was L = 2.28 × 10^{-10} Pa·m^3·s^{-1}, as determined using Eq. (2).

$$R_1 = \frac{LP_E}{P_0}\left(\frac{M_A}{M}\right)^{\frac{1}{2}}\left\{1 - e^{-\left[\frac{LT_1}{VP_0}\sqrt{\left(\frac{M_A}{M}\right)}\right]}\right\}e^{-\left[\frac{LT_2}{VP_0}\sqrt{\left(\frac{M_A}{M}\right)}\right]} \quad (2)$$

where R_1 is the measured leak rate of the tracer gas (He) through the leak, L is the equivalent standard leak rate, P_E = 5.17 × 10^5 Pa is the pressure of exposure, P_0 = 1.01 × 10^5 Pa is the atmospheric pressure, M_A = 28.7 g is the molecular weight of air, M = 4 g is the molecular weight of He, T_1 = 7200 s is the time of exposure to P_E, T_2 = 1800 s is the dwell time between the release of pressure and leak detection, and V = 27 mm^3 is the internal volume of the vapor cell.

The measured leakage rate was significantly higher than the actual leakage rates in air and nitrogen during real operation due to He permeation of the BF33 glass substrate. During the actual operation, the lifetime of the atomic gas chamber must also be assessed. There are several ways to mitigate He permeation, including switching to aluminosilicate glass instead of borosilicate glass [43]. However, this method is expensive. Other options include sputtering an alumina coating on the chamber walls [44] or using gallium phosphide as a sealing material for anode bonding [45]. These methods can significantly prolong the lifetime of atomic vapor cells.

3.5. Absorption spectra and FID signal

A schematic of the test system is shown in Fig. 11(a). This system was used to measure the absorption spectrum of the vapor cell and the FID signals of the different pumping detection schemes. This study aimed to evaluate the effects of the inner sidewalls of molded glass holes on the performance of a vapor cell.

Two non-magnetic heating coils were attached to both sides of the vapor cell in order to heat it to a specified temperature. During the measurement, the vapor cell was placed in a magnetic shielding barrel composed of four layers of permalloy and one layer of manganese–zinc (Mn–Zn) ferrite. As shown in Fig. 11(b), the magnetic fields inside the shields were controlled by three-axis magnetic coils with a set of solenoid coils for the longitudinal field and two sets of cosine-theta coils for the transverse field. In

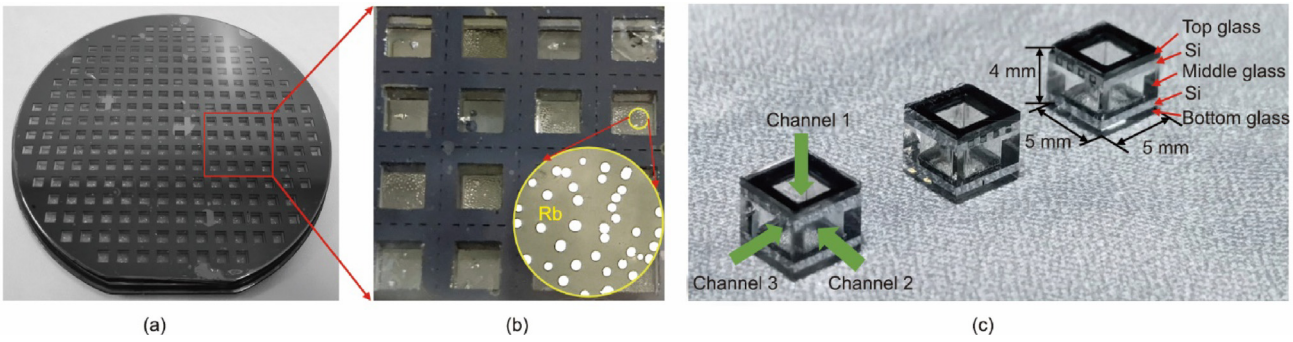

Fig. 10. The fabricated wafer-level alkali metal atomic vapor cells with multi-optical channels. (a) The fabricated wafer. (b) The alkali metal in the vapor cells (inset shows the Rb droplet). (c) The fabricated alkali metal atomic vapor cell with three optical channels.

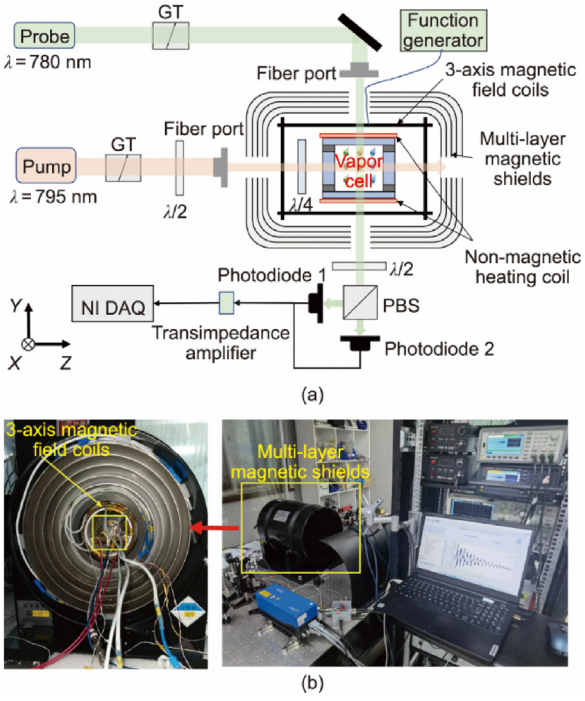

Fig. 11. The dual-beam optical test platform for the characterization of the vapor cells. (a) Schematic of the test platform. (b) Experimental setup, magnetic shields, and three-axis magnetic field coils. GT: Glan–Thompson polarizer; $\lambda/2$: half wave plate; $\lambda/4$: quarter wave plate; PBS: polarizing beam splitter prism; NI DAQ: NI data acquisition card; *X*, *Y*, *Z*: the axes of the Cartesian coordinate system.

addition, a 795 nm circularly polarized light beam was passed through the vapor cell in the *z*-direction to pump the Rb atoms. The Xe nuclear spins were hyperpolarized via spin-exchange optical pumping with Rb atomic spins. Another 780 nm linearly polarized light beam was passed through the vapor cell in the *y*-direction to detect the atomic spin signal. Performing experiments using a free-space laser beam is difficult because the vapor cell is small. Therefore, a polarization-maintaining fiber is used to guide the pump and probe lasers into the vapor cell.

The vapor cell was heated to 393 K to obtain the absorption spectrum. After the temperature of the vapor cell was stabilized, the frequency of the laser was adjusted to set the wavelengths of the pump and probe lasers to approximately 795 and 780 nm, respectively. The output voltages of the photodiode at different tuning frequencies were recorded to obtain the absorption curves, as shown in Fig. 12.

The width of the absorption curve is mainly due to the natural broadening Γ_{nat}, Doppler broadening Γ_G, and pressure broadening

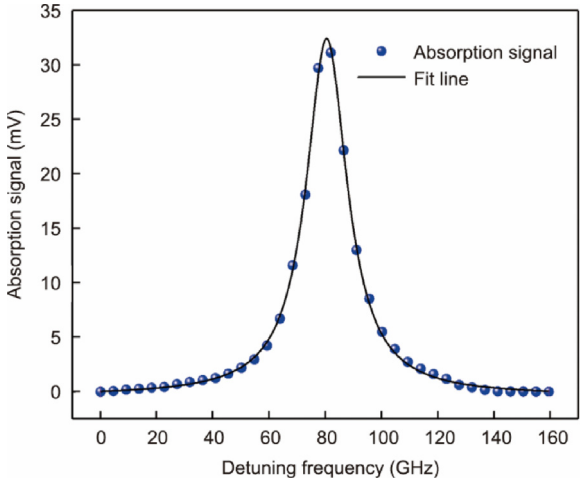

Fig. 12. Absorption spectrum measured in the *D*2 line of the Rb atom. The absorption peak was fitted using a Lorentz function.

Γ_p [46]. The natural broadening of the absorption spectral lines can be calculated using Eq. (3).

$$\Gamma_{nat} = \frac{1}{2\pi\tau} \tag{3}$$

where τ is the natural lifetime of the excited state of an alkali metal atom, which is approximately 25–35 ns. The natural linewidth for the transition of the *D*1 and *D*2 lines of alkali metal atoms is 4–6 MHz. The effect of natural broadening on the absorption spectrum is negligible compared with a pressure broadening of more than 10 GHz.

The Gaussian function of the atomic absorption spectrum under the Doppler effect is given as follows:

$$G(\nu - \nu_0) = \frac{2\sqrt{(\ln 2)/\pi}}{\Gamma_G} \exp\left(\frac{-4(\ln 2) \times (\nu - \nu_0)^2}{{\Gamma_G}^2}\right) \tag{4}$$

where ν is the pump laser detuning frequency, ν_0 = 377 THz is the resonance frequency of Rb, and Γ_G is the spectral linewidth of the Doppler broadening.

$$\Gamma_G = 2\nu_0\sqrt{\frac{2k_B T \ln 2}{mc^2}} \tag{5}$$

where k_B is the Boltzmann constant, T = 393 K is the temperature, m is the mass of Rb, and c is the speed of light. After the calculation, Γ_G = 414 MHz.

The absorption spectrum under pressure broadening conforms to the Lorentz line distribution, which is expressed as follows:

$$L(v - v_0) = a\frac{\Gamma_p/2\pi}{(v - v_0)^2 + (\Gamma_p/2)^2} + b \tag{6}$$

where a and b are fitting coefficients, and Γ_p is the spectral width of the pressure broadening.

As shown in Eq. (7), the absorption data should be fitted using the Voigt function, which is a convolution of a Gaussian function and a Lorentzian function. The Gaussian function accounts for the Doppler broadening, whereas the Lorentzian function estimates the pressure broadening caused by the collision of buffer gases [47].

$$v(v - v_0) = \int_0^\infty L(v - v')G(v' - v_0)\mathrm{d}v' \tag{7}$$

where v' is the integral variable of the convolution, denoting all possible positions in the range $(0, \infty)$.

In this study, the buffer gas pressure was greater than 0.6 atm (1 atm = 1.01325 × 10^5 Pa); thus, the influence of Doppler broadening on the absorption spectrum can be ignored [48,49]. For each Rb isotope, the ground-state hyperfine splitting is greater than 3 GHz. The sum of the four Lorentzian quantities in the form of Eq. (6) was used to fit the absorption spectral data and estimate the pressure broadening Γ_p. At 393 K, $\Gamma_p = 14.16$ GHz was performed by means of Lorentz fitting. From the 18.3 GHz·amg^{-1} [48] (the amg is the numerical density unit of a gas, with 1 amg = 2.6867811 × 10^{25} m^{-3}, defined as the number of molecules of an ideal gas per unit volume at 273.15 K and 1 atm pressure) pressure broadening coefficient of the Rb $D2$ line in N_2, the corresponding pressure at room temperature was found to be approximately 595 Torr, which was close to the buffer gas pressure that filled with 620 Torr during the fabrication process in Section 3.3.

The FID method was used to measure the spin precession signals and relaxation times of ^{129}Xe and ^{131}Xe. The test temperature was set at 393 K. First, a static magnetic field B_0 = 510 nT was applied along the pump axis—that is, the z-axis. This led to a Larmor precession of the nuclear spin along the z-axis and the precession frequency, where is the nuclear gyromagnetic ratio of ^{129}Xe or ^{131}Xe. Then, a π/2 pulsed magnetic field was applied along the y-direction to reflect the magnetization vector of the nuclear spin to the xy plane. A signal proportional to the realignment of the nuclear spin along the z-axis was detected by the probe beam using an Rb magnetometer. Fig. 13 shows the FID and fast Fourier transform (FFT) signals for different pump-detect schemes. The measured FID signals are shown in Figs. 13(a) and (c). Eq. (8) can be used to accurately fit the obtained precession signal by constructing a sinusoidal signal-fitting function for the four frequencies and combining the natural decay exponential process of the spin-precession signal of each frequency component [20,50].

$$f(t) = \sum_{i=1}^{4} M_i e^{-(t-t_0)/T_i} \sin\left[2\pi f_i(t - t_0) + \varphi_i\right] + c \tag{8}$$

where M_i is the amplitude of the transverse magnetization of Xe for each vibration component, the attenuation constant $1/T_i$ of the FID signal amplitude corresponds to the transverse relaxation time of Xe, as shown in Fig. 13, T_i is the transverse relaxation time of ^{129}Xe or ^{131}Xe, t_0 is the initial test time, f_i is the precession frequency of ^{129}Xe or ^{131}Xe with a nuclear quadrupole shift, φ_i is the initial phase of each component, and c is the fitting coefficient.

Figs. 13(b) and (d) show the frequency spectrum obtained by the FFT presented in Figs. 13(a) and (c). The FFT data were then fitted to a quadruple Lorentzian function, which is expressed as follows:

$$f(v) = \sum_{i=1}^{4} A_i \frac{\Gamma_i/2\pi}{(v - v_i)^2 + (\Gamma_i/2)^2} + b \tag{9}$$

where A_i is the amplitude of each vibration component, v_i is the resonance frequency of each vibration component, Γ_i is the resonance

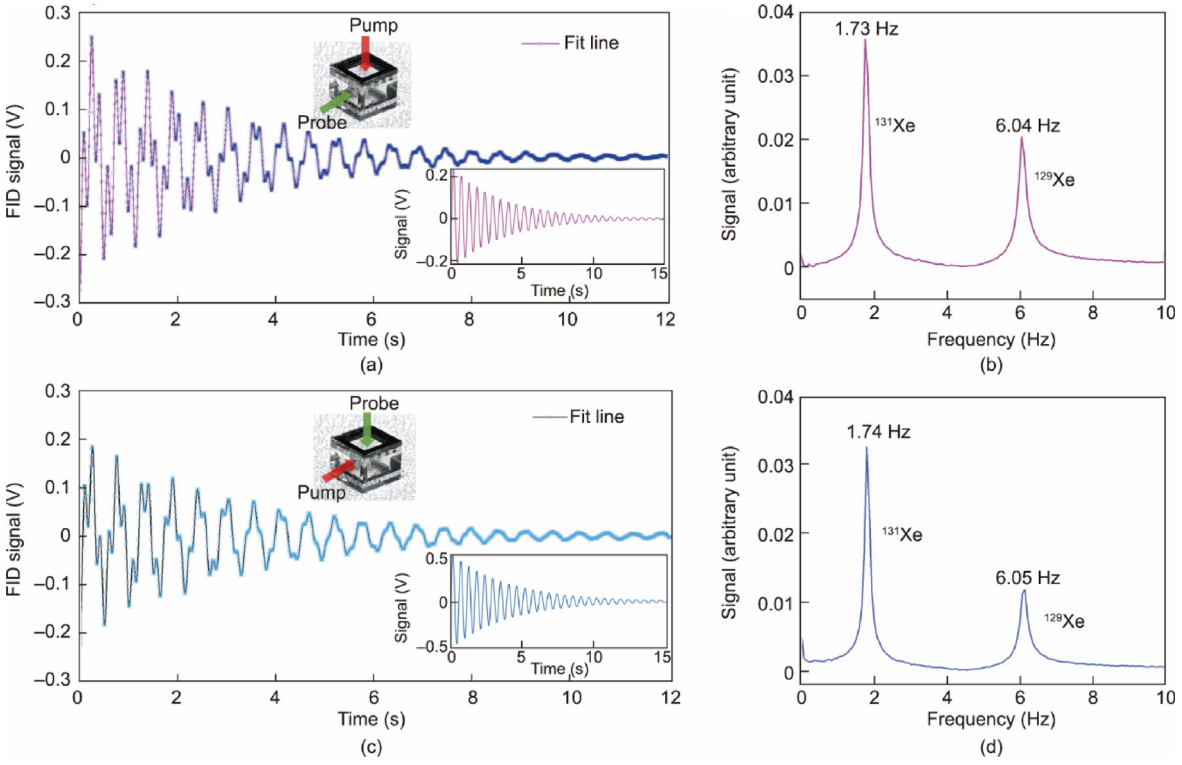

Fig. 13. The FID signal of the transverse ^{129}Xe and ^{131}Xe polarization under different pump and probe schemes. (a) FID signal of the channel 1 pump and the channel 2 or 3 probe (the inset represents the ^{131}Xe spin precession signal extracted from the mixed signal). (b) Fast Fourier transform (FFT) of the FID signal in part (a). (c) FID signal of the channel 2 or 3 pump, and the channel 1 probe (the inset represents the ^{131}Xe spin precession signal extracted from the mixed signal). (d) FFT of the FID signal in part (c).

peak width of each vibration component, respectively, and b is the fitting constant, which is used for the case where the decay center of the FID signal is not zero. The FID and FFT signal fitting codes are available in Appendix A.

Figs. 13(a) and (b) show the signals obtained using channel 1 as the pump channel and channel 2 as the probe channel, respectively. The precession frequency of some atoms shifted because of electric quadrupole splitting during the collision between ^{131}Xe and the vapor cell wall. After fitting, the relaxation times T_2 of ^{129}Xe and ^{131}Xe were 2.04 and 4.47 s, respectively. The Larmor precession frequencies of ^{129}Xe and ^{131}Xe are 6.04 and 1.73 Hz, respectively. The linewidths of the frequency peaks were 0.61 and 0.36 Hz, and the electric quadrupole frequency shift of ^{131}Xe was 52.24 mHz. Figs. 13(c) and (d) show the signal obtained using channel 1 as the probe channel, channel 2 as the pump channel, and the frequency spectrum obtained by the FFT. The T_2 values of ^{129}Xe and ^{131}Xe under this working scheme are 2.09 and 4.92 s, respectively. The Larmor precession frequencies were 6.05 and 1.74 Hz, and the linewidths of the frequency peaks were 0.58 and 0.36 Hz, respectively. The electric quadrupole frequency shift of ^{131}Xe is 43.31 mHz.

4. Discussion

We did not observe the common electric quadrupole splitting peak of ^{131}Xe in the FFT signal spectrum, because the electric quadrupole frequency shift was very small for observation; therefore, the peak of ^{131}Xe is the combination of three resonance peaks. This phenomenon can be explained as follows:

(1) Compared with vapor cells made via the traditional glass-blowing process, which must have a residual stem after the alkali metal injection, the vapor cell used in this study was stemless. The stem breaks the symmetry of the vapor cells, particularly in small cells [19].

(2) The highly symmetric cubic MEMS atomic vapor cell cavity had a significant suppression effect on the electric quadrupole frequency shift of ^{131}Xe [24,51], resulting in a small frequency shift of the energy level. Thus, we observed only a single peak in the ^{131}Xe signal.

(3) Side molding gives the vapor cell a smooth inner surface, further suppressing the electric quadrupole frequency shift compared with the rough inner surface of a conventional MEMS vapor cell cavity formed by means of dry etching [52].

The nuclear spin of ^{131}Xe is 3/2, and the magnetic dipole interacts with the electric quadrupole. In addition, the nuclear spin of ^{129}Xe is 1/2, and only magnetic dipole interactions are allowed. The NMR energy levels of ^{131}Xe and ^{129}Xe are 4 and 2, respectively. In terms of spin arrangement, fewer energy levels can ensure greater polarizability. Theoretically, compared with ^{129}Xe, ^{131}Xe exhibits a smaller magnetization and wider NMR width [20]. However, the NMR linewidth of the ^{131}Xe processed in this study was much smaller than that of ^{129}Xe. It is possible that the polarization gradient of the pump light causes the relaxation time of ^{129}Xe to be shorter than that of ^{131}Xe, leading to a smaller resonance linewidth for ^{131}Xe.

The relaxation time of ^{131}Xe observed in this experiment was small because of the wall relaxation of the ^{131}Xe atoms. The quadrupolar interaction between the cell wall and the ^{131}Xe nuclear spin was the main relaxation process. Filling a small amount of hydrogen (H_2) or deuterium (D_2) into the vapor cell to form RbH or RbD films can effectively prolong the nuclear spin-relaxation time of ^{131}Xe, which will be the focus of our next study.

The FID signals of ^{129}Xe and ^{131}Xe obtained by the two pump–probe schemes show that the multi-optical-channel MEMS alkali metal vapor cell meets the requirements for multi-beam atomic devices. We used optical magnetometer signal amplitudes as a metric to compare different orientations and to estimate the optimal orientation of light coupling to the atomic sensors. The signal amplitudes of the two pump–probe schemes after the tests are shown in Figs. 13(a) and (c). When channel 1 was the pump channel and channel 2 or channel 3 was the probe channel, the signal amplitude of the channel 1 pumping was approximately 1.3 times that of the channel 2 or channel 3 pumping. This difference in the signal amplitude was attributed to a decrease in the lateral transmittance, resulting in a decrease in the pumping efficiency. In the future, we will further optimize the molding process to improve the lateral transmittance.

5. Conclusions

In this study, the batch manufacturing of MEMS alkali-metal atomic vapor cells with multiple optical channels was accomplished using multilayer anodic bonding and precise side-molding technology. A highly transparent vapor-cell sidewall was created using a process that included laser drilling, wet etching, and precision side molding. The required laser wavelength transmittance was approximately 89.5%, the average surface roughness was 22 nm, and the average surface shape accuracy PV was 283 nm. Alkali-metal injection, noble-gas recycling, and recovery systems were developed, and a test platform with a double-path laser was constructed. The absorption spectrum demonstrated the precise control of gas pressure. The developed multi-optical-channel alkali metal vapor cell satisfies the requirements of multi-optical-channel atomic devices, based on the results of the measurement and a comparison of the FID signals of ^{129}Xe and ^{131}Xe of the processed vapor cell under various pump-probe schemes.

Acknowledgments

This work was supported in part by the National Key Research and Development Plan (2022YFB3203400), the National Natural Science Foundation of China (62103324 and U1909221), and the Natural Science Foundation of Shaanxi (2022JQ-554).

Compliance with ethics guidelines

Mingzhi Yu, Yao Chen, Yongliang Wang, Xiangguang Han, Guoxi Luo, Libo Zhao, Yanbin Wang, Yintao Ma, Shun Lu, Ping Yang, Qijing Lin, Kaifei Wang, and Zhuangde Jiang declare that they have no conflict of interest or financial conflicts to disclose.

Appendix A. Supplementary material

Supplementary material to this article can be found online at https://doi.org/10.1016/j.eng.2023.08.016.

References

[1] Kitching J, Knappe S, Donley EA. Atomic sensors—a review. IEEE Sens J 2011;11(9):1749–58.
[2] Degen CL, Reinhard F, Cappellaro P. Quantum sensing. Rev Mod Phys 2017;89(3):035002.
[3] Doherty MW, Manson NB, Delaney P, Jelezko F, Wrachtrup J, Hollenberg LCL. The nitrogen-vacancy colour centre in diamond. Phys Rep 2013;528(1):1–45.
[4] Jaklevic RC, Lambe J, Silver AH, Mercereau JE. Quantum interference effects in Josephson tunneling. Phys Rev Lett 1964;12(7):159–60.
[5] Jaklevic RC, Lambe J, Mercereau JE, Silver AH. Macroscopic quantum interference in superconductors. Phys Rev 1965;140(5A):A1628.
[6] Bell WE, Bloom AL. Optical detection of magnetic resonance in alkali metal vapor. Phys Rev 1957;107(6):1559–65.
[7] Alexandrov EB, Bonch-Bruevich VA. Optically pumped atomic magnetometers after three decades. Opt Eng 1992;31(4):711–7.

[8] Martin KW, Phelps G, Lemke ND, Bigelow MS, Stuhl B, Wojcik M, et al. Compact optical atomic clock based on a two-photon transition in rubidium. Phys Rev Appl 2018;9(1):014019.
[9] Newman ZL, Maurice V, Drake T, Stone JR, Briles TC, Spencer DT, et al. Architecture for the photonic integration of an optical atomic clock. Optica 2019;6(5):680–5.
[10] Godone A, Levi F, Calosso CE, Micalizio S. High-performing vapor-cell frequency standards. Riv Nuovo Cimento 2015;38(3):133–71.
[11] Kominis IK, Kornack TW, Allred JC, Romalis MV. A subfemtotesla multichannel atomic magnetometer. Nature 2003;422(6932):596–9.
[12] Budker D, Romalis M. Optical magnetometry. Nat Phys 2007;3(4):227–34.
[13] Shah V, Knappe S, Schwindt PDD, Kitching J. Subpicotesla atomic magnetometry with a microfabricated vapour cell. Nat Photonics 2007;1:649–52.
[14] Kornack TW, Ghosh RK, Romalis MV. Nuclear spin gyroscope based on an atomic comagnetometer. Phys Rev Lett 2005;95(23):230801.
[15] Sorensen SS, Thrasher DA, Walker TG. A synchronous spin-exchange optically pumped NMR-gyroscope. Appl Sci 2020;10(20):7099.
[16] Bell WE, Bloom AL, Lynch J. Alkali metal vapor spectral lamps. Rev Sci Instrum 1961;32(6):688–92.
[17] Balabas MV, Budker D, Kitching J, Schwindt PDD, Stalnaker JE. Magnetometry with millimeter-scale antirelaxation-coated alkali-metal vapor cells. J Opt Soc Am B 2006;23(6):1001–6.
[18] Castagna N, Bison G, di Domenico G, Hofer A, Knowles P, Macchione C, et al. A large sample study of spin relaxation and magnetometric sensitivity of paraffin-coated Cs vapor cells. Appl Phys B Lasers Opt 2009;96(4):763–72.
[19] Wu Z. Wall interactions of spin-polarized atoms. Rev Mod Phys 2021;93 (3):035006.
[20] Feng YK, Zhang SB, Lu ZT, Sheng D. Electric quadrupole shifts of the precession frequencies of ^{131}Xe atoms in rectangular cells. Phys Rev A 2020;102 (4):043109.
[21] Walker TG, Larsen MS. Spin-exchange-pumped NMR gyros. In: Arimondo E, Lin CC, Yelin SF, editors. Advances in atomic, molecular, and optical physics, 65. Cambridge: Elsevier; 2016. p. 373–401.
[22] Kitching J. Chip-scale atomic devices. Appl. Phys Rev 2018;5(3):031302.
[23] Wu Z, Happer W, Kitano M, Daniels J. Experimental studies of wall interactions of adsorbed spin-polarized ^{131}Xe nuclei. Phys Rev A 1990; 42(5):2774–84.
[24] Donley EA, Long JL, Liebisch TC, Hodby ER, Fisher TA, Kitching J. Nuclear quadrupole resonances in compact vapor cells: the crossover between the NMR and the nuclear quadrupole resonance interaction regimes. Phys Rev A 2009;79(1):013420.
[25] Kitching J, Knappe S, Hollberg L. Miniature vapor-cell atomic-frequency references. Appl Phys Lett 2002;81(3):553–5.
[26] Liew LA, Knappe S, Moreland J, Robinson H, Hollberg L, Kitching J. Microfabricated alkali atom vapor cells. Appl Phys Lett 2004;84(14):2694–6.
[27] Knappe S, Gerginov V, Schwindt PDD, Shah V, Robinson HG, Hollberg L, et al. Atomic vapor cells for chip-scale atomic clocks with improved long-term frequency stability. Opt Lett 2005;30(18):2351–3.
[28] Liew LA, Moreland J, Gerginov V. Wafer-level filling of microfabricated atomic vapor cells based on thin-film deposition and photolysis of cesium azide. Appl Phys Lett 2007;90(11):114106.
[29] Hasegawa M, Chutani RK, Gorecki C, Boudot R, Dziuban P, Giordano V, et al. Microfabrication of cesium vapor cells with buffer gas for MEMS atomic clocks. Sens Actuators A 2011;167(2):594–601.
[30] Maurice V, Rutkowski J, Kroemer E, Bargiel S, Passilly N, Boudot R, et al. Microfabricated vapor cells filled with a cesium dispensing paste for miniature atomic clocks. Appl Phys Lett 2017;110(16):164103.
[31] Vicarini R, Maurice V, Abdel Hafiz M, Rutkowski J, Gorecki C, Passilly N, et al. Demonstration of the mass-producible feature of a Cs vapor microcell technology for miniature atomic clocks. Sens Actuators A 2018;280:99–106.
[32] Bulatowicz M, Griffith R, Larsen M, Mirijanian J, Fu CB, Smith E, et al. Laboratory search for a Long-Range *T*-odd, *P*-odd interaction from axionlike particles using dual-species nuclear magnetic resonance with polarized ^{129}Xe and ^{131}Xe gas. Phys Rev Lett 2013;111(10):102001.
[33] Limes ME, Sheng D, Romalis MV. ^{3}He–^{129}Xe comagnetometery using ^{87}Rb detection and decoupling. Phys Rev Lett 2018;120(3):033401.
[34] Eklund EJ, Shkel AM. Glass blowing on a wafer level. J Microelectromech Syst 2007;16(2):232–9.
[35] Eklund EJ, Shkel AM, Knappe S, Donley E, Kitching J. Glass-blown spherical microcells for chip-scale atomic devices. Sens Actuators A 2008;143 (1):175–80.
[36] Perez MA, Nguyen U, Knappe S, Donley EA, Kitching J, Shkel AM. Rubidium vapor cell with integrated Bragg reflectors for compact atomic MEMS. Sens Actuators A 2009;154(2):295–303.
[37] Perez MA, Kitching J, Shkel AM. Design and demonstration of PECVD multilayer dielectric mirrors optimized for micromachined cavity angled sidewalls. Sens Actuators A 2009;155(1):23–32.
[38] Han R, You Z, Zhang F, Xue H, Ruan Y. Microfabricated vapor cells with reflective sidewalls for chip scale atomic sensors. Micromachines 2018;9(4):E175.
[39] Ming W, Chen Z, Du J, Zhang Z, Zhang G, He W, et al. A comprehensive review of theory and technology of glass molding process. Int J Adv Manuf Technol 2020;107(5,6):2671–706.
[40] Zhang Y, Yan G, You K, Fang F. Study on α-Al_2O_3 anti-adhesion coating for molds in precision glass molding. Surf Coat Technol 2020;391:125720.
[41] schott.com [Internet]. Shanghai: SCHOTT AG; c2023[cited 2020 Aug 20]. Available from: https://www.schott.com/zh-cn/products/borofloat.
[42] keyence.com.cn [Internet]. Shanghai: KEYENCE CORPORATION; c2023[cited 2020 Aug 20]. Available from: https://www.keyence.com.cn/ss/products/microscope/roughness/surface/tab01_e.jsp.
[43] Dellis AT, Shah V, Donley EA, Knappe S, Kitching J. Low helium permeation cells for atomic microsystems technology. Opt Lett 2016;41(12):2775–8.
[44] Karlen S, Gobet J, Overstolz T, Haesler J, Lecomte S. Lifetime assessment of RbN_3-filled MEMS atomic vapor cells with Al_2O_3 coating. Opt Express 2017;25 (3):2187–94.
[45] Dural N, Romalis MV. Gallium phosphide as a new material for anodically bonded atomic sensors. APL Mater 2014;2(8):086101.
[46] Rotondaro MD, Perram GP. Collisional broadening and shift of the rubidium D_1 and D_2 lines ($5^2S_{12}\rightarrow5^2P_{12}$, 5^2P_{32}) by rare gases, H_2, D_2, N_2, CH_4 and CF_4. J Quant Spectrosc Radiat Transfer 1997;57(4):497–507.
[47] Noor RM, Asadian MH, Shkel AM. Design considerations for micro-glassblown atomic vapor cells. J Microelectromech Syst 2020;29(1):25–35.
[48] Romalis MV, Miron E, Cates GD. Pressure broadening of Rb D_1 and D_2 lines by ^{3}He, ^{4}He, N_2, and Xe: line cores and near wings. Phys Rev A 1997;56 (6):4569–78.
[49] Zheng H, Quan W, Liu X, Chen Y, Lu J. Measurement of atomic number of alkali vapor and pressure of buffer gas based on atomic absorption. Spectrosc Spectral Anal 2015;35(2):507–11.
[50] Kwon TM, Mark JG, Volk CH. Quadrupole nuclear spin relaxation of ^{131}Xe in the presence of rubidium vapor. Phys Rev A 1981;24(4):1894–903.
[51] Heimann PA, Greenwood IA, Simpson JH. Quadrupole perturbation effects upon the ^{201}Hg magnetic resonance. II. relaxation due to an anisotropic perturbation. Phys Rev A 1981;23(3):1209–14.
[52] Butscher R, Wackerle G, Mehring M. Nuclear quadrupole interaction of highly polarized gas-phase ^{131}Xe with a glass surface. J Chem Phys 1994;100 (9):6923–33.